Mechanical modelling of folding versus faulting in brittle–ductile wedges

Guy D.H. Simpson

Section of Earth Sciences, University of Geneva, 13 rue des Maraîchers, CH-1205 Geneva, Switzerland

ARTICLE INFO

ABSTRACT

The question of whether layered sequences of sedimentary rock subjected to layer-parallel compression will fold or fault is investigated by means of mechanical modelling using the Finite Element Method. The model consists of a rigid basement, a weak visco-elasto-plastic décollement horizon and a relatively competent elastic–plastic cover sequence. Syntectonic erosion and sedimentation on the surface are included using a diffusion model. Numerical results show that folding is the dominant mode of deformation when the décollement horizon is relatively thick and has a low viscosity, when the upper layer has a relatively high elastic shear modulus and when the total thickness of the sequence is relatively small. If any one of these conditions is not satisfied, faulting dominates. Other parameters such as the angle of internal friction and cohesion influence the style of deformation but have little influence on the boundary between folding and faulting. Results are interpreted in terms of competing deformation instabilities. If fold amplification rates are large, folding dominates over faulting. If on the other hand, fold amplification rates are small, faulting dominates because stresses intersect the failure surface before significant fold amplification can occur.

1. Introduction

It is common knowledge that layered sequences of sedimentary rock subjected to layer-parallel compression at relatively low confining pressure and low temperature may either fold, fault, or both fold and fault. For example, some regions such as the southern Appalachian thrust belt (Harris and Milici, 1977) and the Chartreuse massif in the French Alps (Philippe, 1994) have deformed primarily by thrusting (Fig. 1a). Other regions such as the central Appalachian Plateau (Gwinn, 1964) and the Fars zone in the Zagros (Fakhari, 1994) have deformed primarily by folding (Fig. 1c). These differences in the style of deformation are presumably related to the differences in material properties and/or in the thickness and distribution of layers with different strength (e.g., Pfiffner, 1993; Philippe, 1994; Chester, 2003; Sepehr et al., 2006). For instance, many fold belts contain a weak viscous décollement layer consisting of salt or shale overlain by relatively strong carbonate rocks (Davis and Engelder, 1985; Davis and Lillie, 1993). Thrust belts on the other hand tend to lack thick viscous décollement horizons and occur within relatively homogeneous sequences lacking major changes in mechanical stratigraphy (Philippe, 1994). However, analogue compression experiments performed on brittle–ductile wedges containing a weak basal viscous layer sometimes (though

not always) deform by faulting and not by folding (Cotton and Koyi, 2000; Costa and Vendeville, 2002; Smit et al., 2003; Bonini, 2007). Moreover, folding can also occur in rocks exhibiting elastic–plastic (as opposed to viscous) behaviour (Johnson, 1980; Erickson, 1996). What then controls whether a sequence subjected to layer-parallel compression deforms predominantly by folding or faulting?

Previous studies that have analyzed controls on faulting versus folding have recognised that folding and faulting are different responses of the same idealized material to different loading conditions and properties. For example, on the basis of a linear stability analysis, Johnson (1980) studied folding and faulting of elastic–plastic materials and showed that when single layers of sedimentary rock behave as strain-hardening materials they are unlikely to fold, rather they fault, because contrasts in elasticity and strength properties of sedimentary rocks are low. He also showed that whereas multilayers of these same rocks fault rather than fold if contacts are bonded, they fold if contacts are frictionless or have a low yield strength. Erickson (1996) used a similar approach to Johnson (1980) though he considered layers of finite thickness instead of layers embedded within infinite media. Once again, this study shows that the mechanical behaviour for elastic–plastic material is determined by the plastic hardening modulus and the elastic shear modulus and by the nature of the contacts between different layers. Wissing et al. (2003) investigated the control that different layer thicknesses have on the style of deformation in a numerical model. They showed that folding is favored when the

E-mail address: guy.simpson@unige.ch
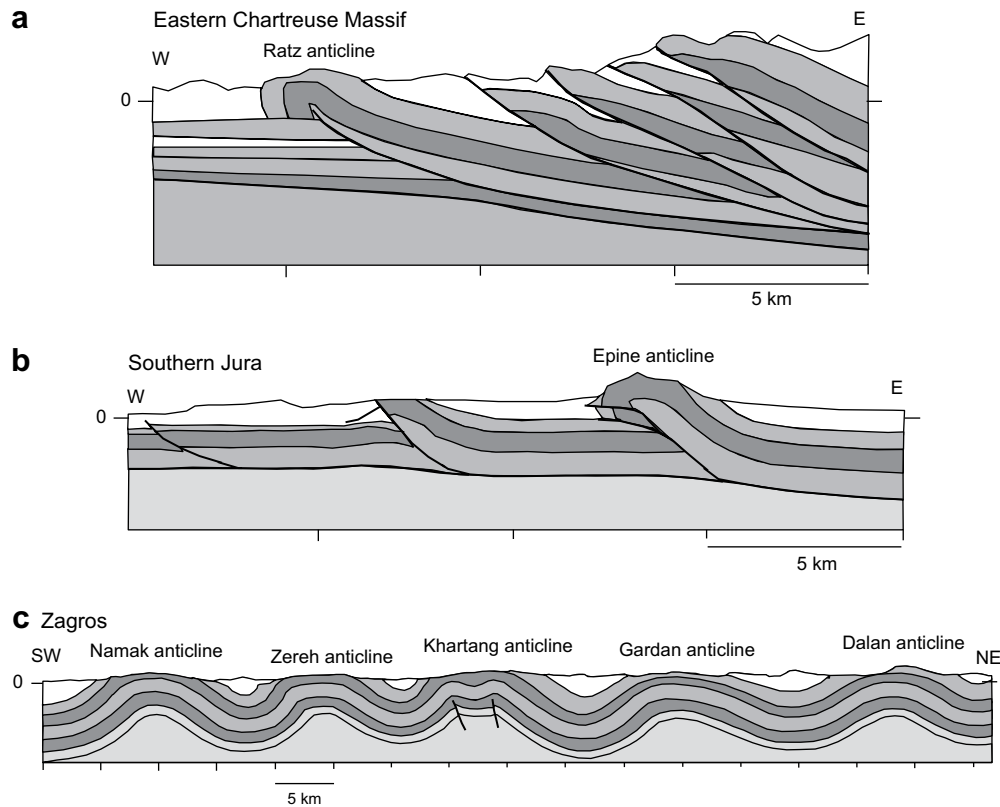
Fig. 1. Examples of cross-sections (no vertical exaggeration) from fold–thrust belts where the deformation is dominated by (a) faulting (Philippe, 1994), (b) folding and faulting (Philippe, 1994) and (c) folding (Fakhari, 1994). The Chartreuse Massif (French Alps) displays typical behaviour characteristic of a strong frictional décollement whereas the Jura (France) was deformed above a viscous detachment consisting of Upper Triassic evaporites. In the Zagros section (from the Khormoj region of the Fars zone, Iran) deformation occurs above a thick décollement zone comprising Paleozoic salt (Hormuz Series).

weak detachment horizon is thick relative to the thickness of individual competent layers, whereas faulting is dominant when the weak detachment is relatively thin. Analogue studies with visco-elasto-plastic materials have showed evidence for both faulting and folding (Dixon and Liu, 1992; Cotton and Koyi, 2000; Costa and Vendeville, 2002; Smit et al., 2003; Bonini, 2007) though the factors controlling the transition between folding and faulting remain poorly understood (Marques, 2008).

Understanding the controls on faulting and folding is complicated by the fact that in many regions, faults and folds are closely related in space and time (Fig. 1b). In such cases, fold/fault relationships are usually classified as one of three end-member styles: fault-bend folding (Suppe, 1983), fault-propagation folding (Suppe and Medwedeff, 1984; Chester and Chester, 1990) and detachment folding (Laubscher, 1977; Jamison, 1987; Dahlstrom, 1990). In these models, folding is normally viewed to be a consequence of, or concurrent with, faulting which is considered as primary (see also Goff et al., 1996 and Gerbault et al., 1999). An alternative possibility is that folds may develop as primary buckling instabilities (Biot, 1961), while faults are secondary features produced after fold locking (Fischer et al., 1992). This is consistent with both analogue (Dixon and Liu, 1992) and theoretical studies (Johnson, 1980; Jamison, 1992; Erickson, 1996) which demonstrate that material response is a competition between two fundamentally different deformation instabilities, folding and faulting.

The purpose of this paper is to better understand the factors controlling the style of deformation in sedimentary sequences subjected to layer-parallel compression. This is achieved by employing a two-dimensional, plane strain mechanical model including visco-elasto-plastic (Mohr–Coulomb) behaviour which is

solved numerically using the Finite Element Method (Simpson, 2006). The model is used to examine the influence of material parameters and mechanical stratigraphy on the nature of deformation and in particular on the transition from faulting to folding. Whereas previous studies focusing on folding versus faulting have been based on linear stability analyses (e.g., Johnson, 1980; Erickson, 1996), field work (e.g., Fischer et al., 1992; Chester, 2003) or analogue modelling (Marques, 2008), the current work appears to be one of the first to attempt a systematic investigation of this problem using full mechanical modelling (see also Wissing et al., 2003).

2. Mechanical model

The mathematical model employed in this study (Fig. 2) is similar to that described by Simpson (2006) but is repeated here for completeness.

2.1. Governing equations

The mechanical model is based on the Stokes equations for slow creeping flow which is weakly compressible (due to elasticity). In two dimensions the governing equations are the conservation of momentum

$$\frac{\partial \sigma_{ij}}{\partial x_i} + \rho g_j = f_j \tag{1}$$

and the conservation of mass
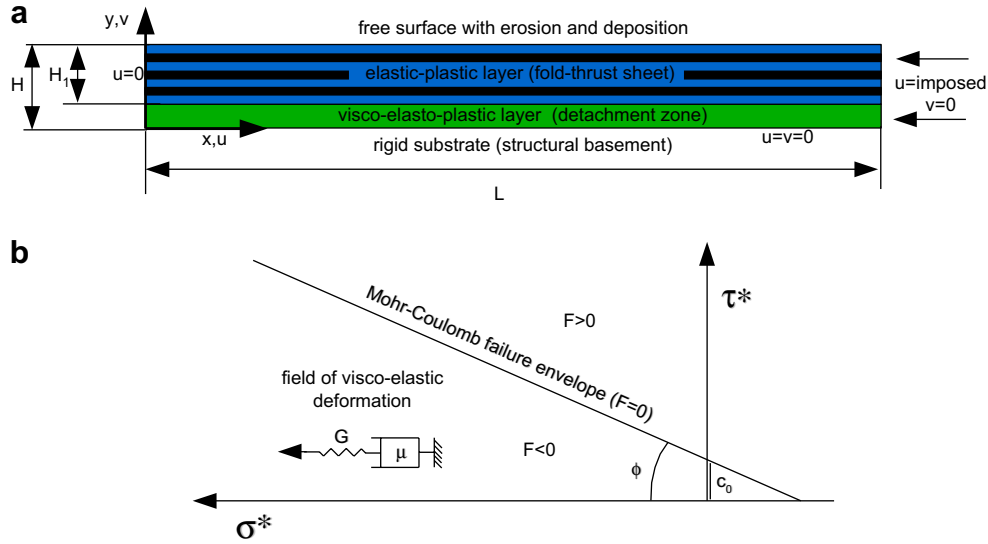
Fig. 2. Schematic diagram of model setup (a) and model rheology (b). The model (not drawn to scale) consists of a relatively competent, homogeneous elasto-plastic layer (with thickness H_1) overlying a weak visco-elasto-plastic décollement (with thickness $H - H_1$). The right hand boundary is moved to the left with a constant velocity generating deformation in the layered sequence. A no-slip condition is imposed at the interface between the weak layer and the rigid basement. The blue and black layers in the upper unit are passive markers and do not have different properties. Deformation is elastic (in the upper layer) or visco-elastic (in the lower layer) when stresses are below the Mohr–Coulomb failure envelope (i.e., $F < 0$) whereas it is also plastic when stresses satisfy the failure condition (i.e., $F = 0$). Stresses are returned to the failure envelope assuming non-associated plasticity with a dilatancy angle of zero. (For interpretation of the references to colour in this figure legend, the reader is referred to the web version of this article.)

$$\frac{\partial u_i}{\partial x_i} + \frac{\partial P}{\partial t}\frac{1}{K} = 0 \qquad (2)$$

where σ_{ij} is the stress tensor (negative in compression), u_i is the velocity vector, P is the rock pressure, ρ is the density, K is the elastic bulk modulus, g_j is the acceleration due to gravity in the jth direction, f_j are additional loads (e.g., due to plastic deformation) and the indices i and j take on the values 1 and 2 (see Table 1 for notation).

A coordinate system is adopted whereby x is horizontal and y is vertical. Before introducing the rheological relations it is convenient to decompose the stress and strain tensors into their dilatational and deviatoric parts as follows

$$\sigma_{ii} = \sigma_{xx} + \sigma_{yy} + \sigma_{zz} \qquad (3)$$

$$\tilde{\sigma}_{ij} = \sigma_{ij} - \frac{1}{3}\sigma_{ii}\delta_{ij} \qquad (4)$$

$$\epsilon_{ii} = \epsilon_{xx} + \epsilon_{yy} + \epsilon_{zz} \qquad (5)$$

$$\tilde{\epsilon}_{ij} = \epsilon_{ij} - \frac{1}{3}\epsilon_{ii}\delta_{ij} \qquad (6)$$

where tildes refer to deviatoric components and δ_{ij} is the Kronecker Delta which is 1 when $i = j$ and 0 when $i \neq j$. In addition, the rock pressure (positive in compression) is defined as

$$P = -\frac{1}{3}\sigma_{ii} \qquad (7)$$

The rheology considered is visco-elasto-plastic (Fig. 2). It is assumed that deviatoric components of deformation are governed by the Maxwell visco-elastic model (see also Moresi et al., 2003).

$$\frac{\partial \tilde{\epsilon}_{ij}}{\partial t} = \frac{\widehat{\sigma}_{ij}}{2G} + \frac{\tilde{\sigma}_{ij}}{2\mu} \qquad (8)$$

where G is the elastic shear modulus, μ is the shear viscosity and $\widehat{\sigma}_{ij}$ is the Jaumann corotational deviatoric stress rate defined as

$$\widehat{\sigma}_{ij} = \frac{\partial \tilde{\sigma}_{ij}}{\partial t} + \frac{1}{2}\Big(w_{ik}\tilde{\sigma}_{kj} - \tilde{\sigma}_{ik}w_{kj}\Big) \qquad (9)$$

where $i,j,k = 1,2$ and w is the material spin tensor with the form

$$w_{ij} = \frac{\partial u_j}{\partial x_i} - \frac{\partial u_i}{\partial x_j} \qquad (10)$$

Table 1
Notations.

Symbol	Unit	Explanation
σ_{ij}	Pa	Total stresses
P	Pa	Rock pressure
$\tilde{\sigma}_{ij}$	Pa	Deviatoric stresses
$\dot{\epsilon}_{ij}$	s^{-1}	Total strain rates
$\dot{e}$	s^{-1}	Imposed strain rate
ϵ_{ij}	–	Total strains
$\tilde{\epsilon}_{ij}$	–	Deviatoric strains
x,y	m	Spatial coordinates
t	s	Time
u,v	$m\,s^{-1}$	Rock velocities
μ	Pa s	Shear viscosity
K	Pa	Bulk modulus
G	Pa	Shear modulus
c_0	Pa	Cohesive strength of intact rock
ϕ	–	Angle of internal friction
ϕ_b	–	Angle of internal friction in viscous layer
χ	–	Ellipticity of finite strain ellipse
γ	–	Strain weakening parameter
ρg	$kg\,m^{-2}\,s^{-2}$	Specific weight
h	m	Elevation of the free surface
κ	$m^2\,s^{-1}$	Surface process diffusivity
H	m	Initial thickness of model
H_1	m	Initial thickness of upper (elasto-plastic) layer
L	m	Initial length of model
R	–	$\mu\dot{e}/K$
S	–	G/K
B	–	$\rho g H/K$
C	–	c_0/K
T	–	H_1/H
E	–	$\kappa/H^2\dot{e}$

Introducing Equation (9) into (8) and discretising the stress derivative with an implicit finite difference approximation lead to the following update equation for deviatoric stresses

$$\tilde{\sigma}_{ij} = \eta \frac{\partial \tilde{\epsilon}_{ij}}{\partial t} + \eta \theta \tilde{\sigma}_{ij}^0 + \frac{\eta \theta dt}{2}\left(w_{ik}^0 \tilde{\sigma}_{kj}^0 - \tilde{\sigma}_{ik}^0 w_{kj}^0\right) \quad (11)$$

where superscripts with 0 refer to quantities from the previous time step, dt is the time step, η is the effective viscosity defined as

$$\eta = \frac{1}{1/2\mu + \theta} \quad (12)$$

and

$$\theta = \frac{1}{2Gdt} \quad (13)$$

Volumetric deformation is modeled with a pure elastic model

$$\sigma_{ii} = 3K\epsilon_{ii} \quad (14)$$

where K is the elastic bulk modulus. Differentiating with respect to time and introducing the definition of pressure yield

$$\frac{\partial P}{\partial t} = -K\left(\dot{\epsilon}_{xx} + \dot{\epsilon}_{yy} + \dot{\epsilon}_{zz}\right) \quad (15)$$

which leads to the following pressure update equation

$$P = P^0 - dtK\left(\dot{\epsilon}_{xx} + \dot{\epsilon}_{yy} + \dot{\epsilon}_{zz}\right) \quad (16)$$

where P^0 is the rock pressure from the previous time step. Plastic deformation is modeled with pressure sensitive Mohr–Coulomb behaviour governed by the following yield function

$$F = \tau^* + \sigma^* \sin\phi - c\cos\phi \quad (17)$$

where c is the cohesive rock strength, ϕ is the angle of internal friction,

$$\sigma^* = \frac{1}{2}(\sigma_{xx} + \sigma_{yy}) \quad (18)$$

and

$$\tau^* = \sqrt{\frac{1}{4}(\sigma_{xx} - \sigma_{yy})^2 + \sigma_{xy}^2} \quad (19)$$

Deformation is visco-elastic when $F < 0$ and plastic when $F \geq 0$, requiring stresses to be reduced such that $F = 0$ (Fig. 2b). Plasticity is assumed to be non-associated with a dilatancy angle of zero, implying no plastic volumetric strain. This formulation leads to a particularly simple algorithm to return stresses of plastic points to the yield surface

$$\sigma_{xx} = \sigma^* + \frac{1}{2}(\sigma_{xx} - \sigma_{yy})\beta \quad (20)$$

$$\sigma_{yy} = \sigma^* - \frac{1}{2}(\sigma_{xx} - \sigma_{yy})\beta \quad (21)$$

$$\sigma_{xy} = \sigma_{xy}\beta \quad (22)$$

where all stresses on the right hand side of Equations (20)–(22) are understood to be old stresses (i.e., $F > 0$), whereas stresses on the left satisfy $F = 0$, and

$$\beta = \frac{|c\cos\phi - \sigma^* \sin\phi|}{\tau^*} \quad (23)$$

The difference between old stresses and new stresses on the failure surface can be thought of as plastic stresses. These can be used to compute out-of-balance plastic forces which can be added to the right hand side load vector f in Equation (1). Thus, the approach followed here is to perform repeated visco-elastic solutions with stresses satisfying the plastic failure criteria and to achieve convergence by iteratively varying the load vector f.

Strain weakening is incorporated by decreasing the cohesion in a nonlinear fashion according to the function

$$c = \frac{c_0}{1 + \frac{(\chi-1)^2}{\gamma}} \quad (24)$$

where χ is the ellipticity of the finite strain ellipse, γ is a non-dimensional parameter describing how rapidly the cohesion decreases as a function of strain and c_0 is the cohesive strength of intact rock. This simple law accounts for the fact that intact rock has a finite cohesive strength whereas preexisting fractures do not. Note that although strain localisation occurs even when no strain weakening is included, it is incorporated here to enhance localisation and therefore to highlight the difference between folds and faults.

Mass transport is incorporated on the upper surface of the mechanical model using a linear diffusion equation (Culling, 1964). When considered in the coordinate frame of the deforming upper surface this equation can be written as

$$\frac{\partial h}{\partial t} = \kappa \frac{\partial^2 h}{\partial x^2} \quad (25)$$

where h is the surface elevation and κ is a surface process diffusivity. Implicit in this model is that the sediment flux is linearly (inversely) proportional to the local topographic slope.

2.2. Numerical implementation

Combining the main governing equations leads to three relations (Equation (2) and the 2 equations of Equation (1)) for three unknowns, two velocities and pressure. These equations are solved using the Galerkin Finite Element Method (Zienkiewicz and Taylor, 2000) with a Lagrangian scheme using marker particles (see Sulsky et al., 1995; Gerya and Yuen, 2003 for notation). This formulation consists of two representations for the continuum, one based on marker particles and the other based on the computational grid. The marker particles are tracked throughout deformation and provide a Lagrangian description that can sustain large deformation. Marker particles carry material properties without error while they are advected. They also carry stresses, strains and any other variables related to the deformation history. The computation grid contains no permanent information and is continually modified to track the external boundaries of the model domain. It is only used to determine spatial gradients and to compute the new solution. Information is continuously passed between the marker particles and the computational grid using interpolation. Numerical diffusion is minimized during the update of history variables (e.g., stresses) on marker points by only interpolating changes in the variable rather than the entire variable itself (e.g., see also Gerya and Yuen, 2003). Elements used were nine-node quadrilaterals for velocities and four-node quadrilaterals for pressure, which are assumed to be discontinuous. All calculations presented were performed using 100 elements in the horizontal direction and 20 elements in the vertical direction. The number of marker particles was a factor of 6 greater than the element resolution in each direction. Increasing the resolution leads to sharper shear-zones but changes little of the overall behaviour. The diffusion equation

was also solved using the Galerkin Finite Element Method but using linear weighting and shape functions and a total of ∼600 elements.

2.3. Boundary and initial conditions

Numerical solutions were computed with the following boundary conditions (Fig. 2a): The right hand boundary was moved to the left at a constant velocity (while the vertical velocity is set to zero), no slip in both the horizontal and vertical directions was imposed along the bottom boundary, the upper boundary is treated as a free surface and the left hand boundary was fixed in the horizontal direction, while allowing free slip in the vertical direction. Initial condition consisted of a lithostatic pressure distribution and a horizontal upper surface. The sediment flux at both the left and right boundaries was assumed to be zero. While the model contains no variations in material properties, the fact that vertical velocities are zero at the pushed boundary introduce a heterogeneity which ensures that the deformation does not remain homogeneous.

2.4. Parameters and scaling

A simple two layer model consisting of an elasto-plastic sequence overlying a weaker visco-elasto-plastic layer (Fig. 2a) requires at least 12 physical parameters: $\dot{e}$ (imposed strain rate), G (elastic shear modulus), K (bulk modulus), c_0 (cohesion of intact rock), γ (cohesion weakening parameter), ϕ (angle of internal friction in upper layer), ϕ_b, (angle of internal friction in lower layer), ρg (specific weight), μ (viscosity), H_1 (thickness of upper layer), H (total thickness), κ (surface process diffusivity). Material parameters are considered to vary between the upper and lower layers but are constant within each respective layer.

In order to study the general behaviour of the governing equations and to reduce the number of independent parameters it is usual to compute solutions in non-dimensional form. To non-dimensionalise the governing equations, the following characteristic scales are adopted for time, stress, and length:

$$\text{time} = \frac{1}{\dot{e}} \qquad (26)$$

$$\text{stress} = K \qquad (27)$$

$$\text{length} = H \qquad (28)$$

where $\dot{e}$ is the imposed horizontal strain rate, K is the bulk modulus and H is the initial total thickness of sequence. Scaling the governing equations leads to the following 9 dimensionless parameters: $\mathbf{R} = \eta\dot{e}/K$, $\mathbf{S} = G/K$, $\mathbf{B} = \rho gH/K$, $\mathbf{C} = c_0/K$, $\mathbf{T} = H_1/H$, $\mathbf{E} = \kappa/(H^2\dot{e})$, γ, ϕ and ϕ_b (see Table 1). The most important parameters for this study are the dimensionless viscosity $\mathbf{R}$, the normalised elastic shear resistance $\mathbf{S}$ (ratio of elastic shear modulus to volumetric modulus), the gravity parameter $\mathbf{B}$ and the thickness ratio $\mathbf{T}$. Parameter values for the various model runs are listed in Table 2. The initial aspect ratio of the model was assumed to be 40 (i.e., $L/H = 40$).

All results presented in the following section are presented in non-dimensional form. These can easily be converted to dimensional form once characteristic scales are chosen. For example, if the initial thickness of the model domain H (the characteristic length scale) is chosen to be 3000 m and the imposed strain rate $\dot{e}$ (the inverse of the characteristic time scale) is chosen to be $10^{-15}\,\text{s}^{-1}$, then a non-dimensional uplift rate $\bar{v}$ of 16 equates to $v \sim 1.5$ mm/year (i.e., $v = \bar{v}H\dot{e}$).

3. Numerical results

More than 140 compression experiments have been performed to better understand controls on the style of deformation in brittle–ductile wedges. Of these experiments, 34 different simulations are presented here. Two main modes of deformation are recognised which can be associated with faulting and folding. Note, however the developed faults are strictly continuum features due to the continuous nature of the solution technique (i.e., FEM).

This section begins with a brief description of the primary characteristics pertaining to these different end-member modes. This is followed by a more detailed investigation of the parameters which influence the transition between faulting and folding. Attention is focused on effects due to the variations in viscosity, elastic shear resistance, cohesion and angle of internal friction, along with changes in the relative and total thicknesses of the layered sequence. The reader is referred to Simpson (2006) for a study on the influence of erosion and sedimentation on deformation which is not treated further here.

3.1. General characteristics of faulting and folding

When an elastic–plastic layer is compressed over a weak (low viscosity) décollement horizon the upper layer sometimes deforms in a discontinuous manner that can be identified with faulting (Fig. 3). Faulting in the simulations is characterised by shear localisation leading to the formation of asymmetrical structures and piggy-back basins. In the simplest case, deformation begins near the (right hand) moving boundary and steps towards the foreland (leftward) as new structures are progressively nucleated. The result is the formation of a triangular-shaped wedge comprising multiple foreland-verging thrusts and basins. Faults are generally most active near the deformation front where vertical rock uplift rates are the highest. However, episodic deformation continues to occur well behind the deformation front as the thrust wedge readjusts to accretion of new sediments and to surface mass redistribution.

Under some conditions (outlined in more detail below), the compression of an elastic–plastic layer over a low viscosity décollement horizon leads to continuous deformation that can be identified with folding (Fig. 4). These folds occur where the upper, relatively strong layer deforms into a series of periodic, almost symmetrical anticlines and synclines. Folds initially nucleate serially and propagate from the hinterland towards the foreland. However, in marked contrast to faults, the folds propagate laterally rapidly and quickly become established over the entire domain where they form a series of low-amplitude undulations. While the absolute uplift rates at the surface are similar to when faulting is observed, the zone over which uplift is occurring at any one time tends to be considerably wider during folding than faulting. Subsequent deformation involves fold amplification and progressive localisation onto the earliest-formed structures which may become asymmetrical as fold limbs begin to fail by faulting.

3.2. Controls on folding versus faulting

Simulations indicate that folding is the dominant mode of deformation when the décollement horizon has a relatively low viscosity, when the competent elastic–plastic upper layer is relatively thin compared to the thickness of the viscous substrate, when the upper layer has a high elastic resistance and when the total thickness of the sequence is relatively thin. If any of these conditions are not satisfied, faulting dominates. Several examples of transitions from folding to faulting are illustrated in Figs. 5–8. For instance, whereas folding dominates for high values of the

Table 2
Summary of model runs presented. The following parameter values were constant in all runs: $\gamma = 1$, $\mathbf{E} = 0.1$. All non-dimensional parameters are defined in Table 1.

Model no.	Figure no.	R	S	B	T	C	ϕ	ϕ_b
r80	Fig. 3	6.3×10^{-6}	0.23	0.0088	0.85	0.0024	30°	30°
r44	Fig. 4	6.3×10^{-8}	4.62	0.0088	0.7	0.0024	30°	30°
r44_30	Fig. 5a	6.3×10^{-8}	4.62	0.0088	0.7	0.0024	30°	30°
r48_30	Fig. 5a	6.3×10^{-8}	2.31	0.0088	0.7	0.0024	30°	30°
r47_30	Fig. 5a	6.3×10^{-8}	0.46	0.0088	0.7	0.0024	30°	30°
r43_30	Fig. 5a	6.3×10^{-8}	0.23	0.0088	0.7	0.0024	30°	30°
r24_20	Fig. 5b	6.3×10^{-8}	23.08	0.0088	0.6	0.0024	30°	30°
r7_20	Fig. 5b	6.3×10^{-8}	4.62	0.0088	0.6	0.0024	30°	30°
r27_20	Fig. 5b	6.3×10^{-8}	2.3	0.0088	0.6	0.0024	30°	30°
r126_30	Fig. 6a	6.3×10^{-8}	0.23	0.0088	0.9	0.0024	30°	30°
r125_30	Fig. 6a	6.3×10^{-8}	0.23	0.0088	0.8	0.0024	30°	30°
r122_30	Fig. 6a	6.3×10^{-8}	0.23	0.0088	0.7	0.0024	30°	30°
r124_30	Fig. 6a	6.3×10^{-8}	0.23	0.0088	0.6	0.0024	30°	30°
r116_30	Fig. 6a	6.3×10^{-8}	0.23	0.0088	0.5	0.0024	30°	30°
r105_40	Fig. 6b	6.3×10^{-8}	0.46	0.0088	0.9	0.0024	30°	30°
r39_40	Fig. 6b	6.3×10^{-8}	0.46	0.0088	0.8	0.0024	30°	30°
r47_40	Fig. 6b	6.3×10^{-8}	0.46	0.0088	0.7	0.0024	30°	30°
r117_30	Fig. 7	6.3×10^{-8}	0.46	0.0176	0.5	0.0024	30°	30°
r118_30	Fig. 7	6.3×10^{-8}	0.46	0.0132	0.5	0.0024	30°	30°
r116_30	Fig. 7	6.3×10^{-8}	0.46	0.0088	0.5	0.0024	30°	30°
r119_30	Fig. 7	6.3×10^{-8}	0.46	0.0066	0.5	0.0024	30°	30°
r19_30	Fig. 7	6.3×10^{-8}	0.46	0.0044	0.5	0.0024	30°	30°
r113_22	Fig. 8a	6.3×10^{-6}	2.3	0.0088	0.4	0.0024	30°	30°
r143_22	Fig. 8a	6.34×10^{-7}	2.3	0.0088	0.4	0.0024	30°	30°
r27_22	Fig. 8a	6.34×10^{-8}	2.3	0.0088	0.4	0.0024	30°	30°
r83_40	Fig. 8b	6.34	2.3	0.0088	0.85	0.0024	30°	0°
r76_40	Fig. 8b	6.34×10^{-5}	2.3	0.0088	0.85	0.0024	30°	0°
r80_40	Fig. 8b	6.34×10^{-6}	2.3	0.0088	0.85	0.0024	30°	0°
r77_40	Fig. 8b	6.34×10^{-7}	2.3	0.0088	0.85	0.0024	30°	0°
r68	Fig. 9	6.34×10^{-6}	0.46	0.0088	0.4	0.0024	30°	30°
r96_25	Fig. 10	6.3×10^{-7}	0.46	0.0088	0.7	0.006	30°	30°
r100_25	Fig. 10	6.3×10^{-7}	0.46	0.0088	0.7	0.0024	30°	30°
r95_25	Fig. 10	6.3×10^{-7}	0.46	0.0088	0.7	0.0012	30°	30°
r92_30	Fig. 11	6.3×10^{-8}	0.23	0.0088	0.8	0.0024	40°	40°
r13_30	Fig. 11	6.3×10^{-8}	0.23	0.0088	0.8	0.0024	20°	20°
r90_30	Fig. 11	6.3×10^{-8}	0.23	0.0088	0.8	0.0024	10°	10°

normalised elastic shear modulus, decreasing the elastic shear resistance causes the deformation belt to become narrower while individual structures become progressively more localised and asymmetrical related to faulting (Fig. 5a). Similarly, by increasing the relative thickness of the upper layer (Fig. 6a), by increasing the importance of gravity (e.g., increasing the total thickness of the sequence, Fig. 7) or by increasing the viscosity in the décollement layer (Fig. 8a) one passes from distributed folding to faulting. Fig. 8b illustrates the point that simply the presence of a low viscosity décollement is generally insufficient to ensure that deformation takes place by folding. In this example, due to the both relatively low elastic shear resistance of the upper layer and fact that the décollement is relatively thin (compared to the simulation in Fig. 8a), deformation is accommodated entirely by faulting, even when the detachment horizon has a low viscosity.

Although it is relatively straightforward in these examples to distinguish between folding and faulting, this is not always so. In some cases, one observes no clear separation in space between folding and faulting – i.e., parts of the domain may deform symmetrically by folding whereas other parts deform by localised asymmetrical faulting at the same time. In other instances, folds may be observed to form first before the same structures evolve subsequently by faulting. Sometimes, whether the actual structures themselves are forming by folding or faulting at any one time is ambiguous – i.e., one observes the formation of fold-like structures which have sheared limbs. These features (e.g., see Fig. 9) illustrate the complicated nature of, and close relationship between, folding and faulting. Moreover, considered together with the large number of controlling parameters, they make it difficult to precisely define (in a predictive sense) the boundary between folding and faulting.

3.3. Factors influencing the style of deformation

The style of faulting in ductile-frictional wedges is strongly influenced by the viscosity and thickness of the décollement zone and the thickness of the upper competent layer. Steep narrow wedges with strongly localised structures tend to be associated with relatively high viscosities (Fig. 8b) and/or thin décollement zones (Fig. 6b). In addition, high values of cohesion and angle of internal friction (for the upper competent layer and décollement zone) favor greater strain localisation and therefore steeper, narrower wedges (Figs. 10 and 11). Purely friction wedges display similar features, though individual structures show a strong tendency to verge towards the foreland compared with their viscous counterparts whose structures are more symmetrical, including forethrusts and backthrusts (see Fig. 8b).

As with faulting, the nature of folding depends on various physical parameters, the most important of which are thickness and elastic shear resistance of the upper competent unit, the thickness and viscosity of the décollement horizon and gravity.
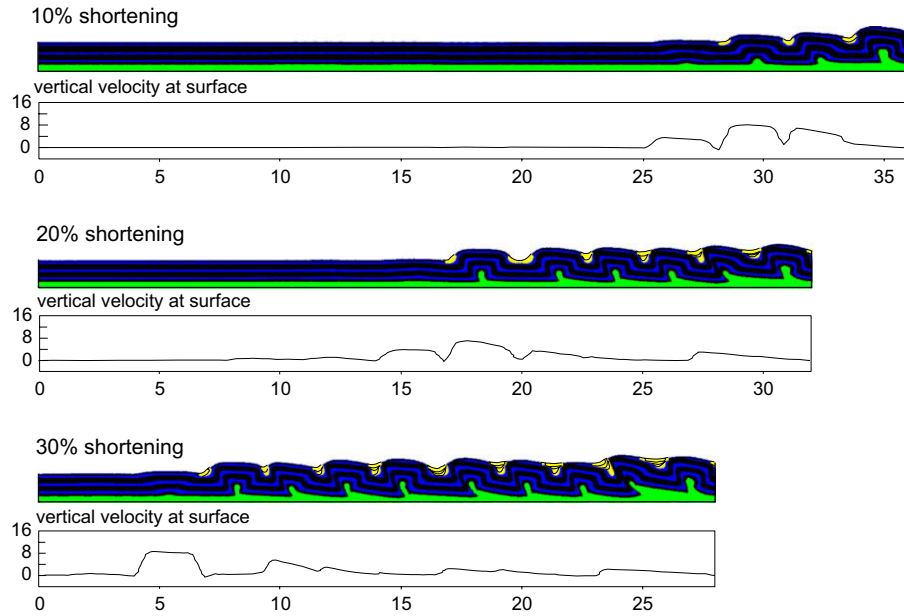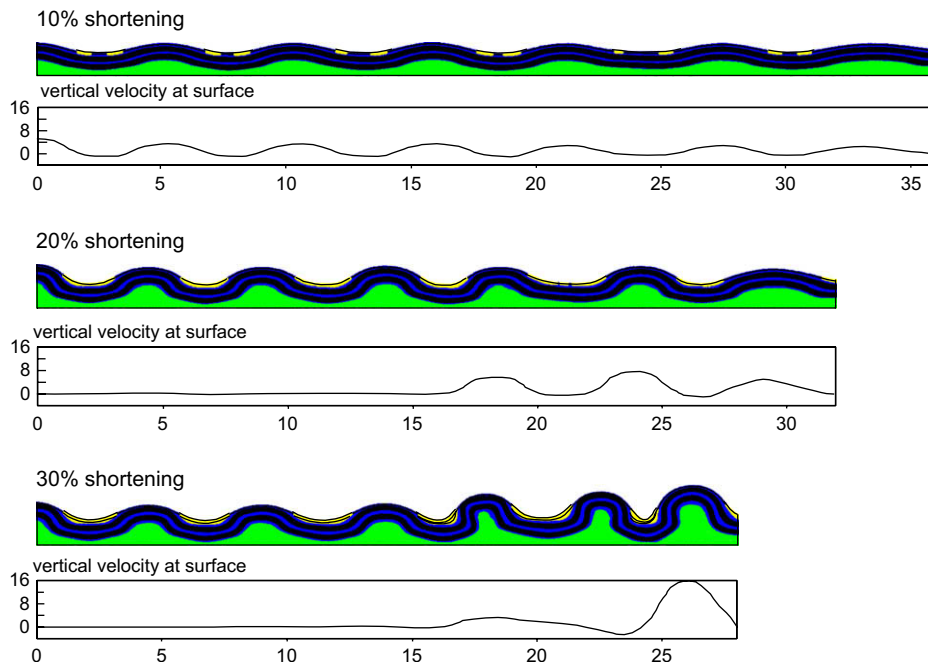
Fig. 3. Deformed cross-sections and distribution of vertical rock uplift rates at the surface as a function of horizontal distance after 10, 20 and 30% of convergence (no vertical exaggeration) for a simulation where faulting is the dominant mode of deformation (cf Fig. 4). Sediment deposited during deformation is shaded yellow (contours indicate deformed stratigraphy). Parameter values are listed in Table 2. (For interpretation of the references to colour in this figure legend, the reader is referred to the web version of this article.)

Both the fold wavelength and the rate of fold growth increase as the elastic resistance increases (Fig. 5b) and the importance of gravity decreases (Fig. 7). As the thickness ratio H_1/H decreases (i.e., the thickness of the décollement horizon becomes thick compared to the upper competent layer) the wavelength decreases whereas the fold growth rate increases (Fig. 6a). The viscosity of the décollement zone has little effect on the fold wavelength but significantly influences the fold growth rate (Fig. 8a).

4. Discussion

One of the primary motivations for this study was to provide an answer to the question: what determines whether a sequence of sedimentary rock subjected to layer-parallel compression will predominantly fold or fault? Results of mechanical modelling provide a partial answer to this question in that it has helped to identify the main parameters controlling the boundary between

Fig. 4. Deformed cross-sections and distribution of vertical rock uplift rates at the surface as a function of horizontal distance after 10, 20 and 30% of convergence (no vertical exaggeration) for a simulation where folding is the dominant mode of deformation (cf Fig. 3). Parameter values are listed in Table 2.

a S=4.62

r44_30

S=2.31

r48_30

S=0.46

r47_30

S=0.23

r43_30

Increasing elastic shear resistance

b S=23.08

r24_20

S=4.62

r7_20

S=2.31

r27_20

Increasing elastic resistance
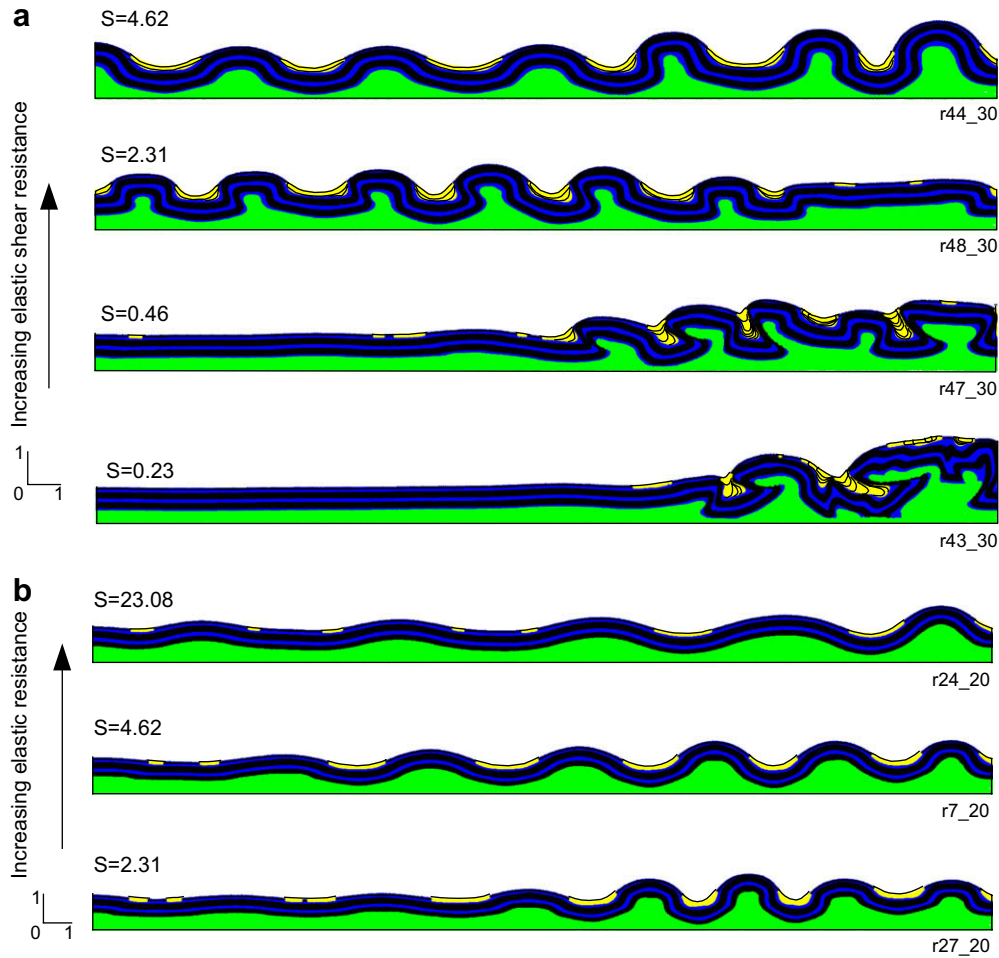
Fig. 5. Influence of the elastic shear resistance **S** on deformation in 2 sets of simulations (parameter values are listed in Table 2). In (a), folding occurs when the rocks have a high elastic shear resistance (e.g., high shear modulus) whereas faulting dominates as the stiffness is reduced (cross-sections show deformation after 30% convergence). The simulations in (b) have a greater décollement zone thickness (**T** = 0.6) than that in (a) (**T** = 0.7). In this case, deformation takes place solely by folding (cross-sections show deformation after 20% convergence).

folding and faulting. In particular, folding dominates when the décollement horizon has a relatively low viscosity, when the competent elastic–plastic upper layer is relatively thin compared to the thickness of the viscous substrate, when the upper layer has a high elastic resistance and when the total thickness of the sequence is relatively thin. Otherwise faulting dominates.

These results can be interpreted in terms of competing deformation instabilities. Consider a simple visco-elastic two-layered sequence containing small amplitude irregularities subjected to layer-parallel compression. Linear instability analyses (e.g., see Biot, 1961) show that the amplitude of preexisting perturbations evolves exponentially as a function of time at different rates (i.e., some wavelengths will grow or decay more rapidly than others). The wavelength which grows the fastest is known as the dominant wavelength. The growth rate of the dominant wavelength is important for determining the nature of deformation that will eventually be observed after a finite amount of deformation. If the maximum growth rate is large, folds will rapidly appear in the competent layer. If, on the other hand, the maximum growth rate is small (and positive), significant amplification will take a long time and folding may be completely masked by shortening and homogeneous thickening of the competent layer. Now consider the additional possibility that the upper competent layer can also deform plastically leading to the formation of faults. What occurs will depend on the competition between folding and faulting.

Folding will be the dominant mode of deformation if the maximum growth rate for folding is large, otherwise faulting will occur.

This reasoning implies that the boundary between folding and faulting will essentially be determined by the parameters controlling the growth rate for the folding of an elasto-plastic layer above a viscous décollement. While a complete analysis of this problem is beyond the scope of this study some useful results have already been published. For example, several studies have investigated the instability of compressed (under pure shear) elastic films above viscous detachments in the absence of gravity (Huang and Suo, 2002a,b). In the limit where the thickness of the viscous layer is small, the growth rate is (Huang and Suo, 2002b):

$$\alpha = \frac{EkH_e(EH_v)^3}{144\mu(1-v^2)}(12\epsilon_0(1+v) - (kH_e))^2 \quad (29)$$

where H_e is the thickness of the upper elastic layer, H_v is the thickness of the viscous layer, μ is the viscosity of the lower weak layer, E is Young's modulus, v is Poisson's ratio, ϵ_0 is the initial strain (here assumed to be positive in compression) and k is the wavenumber of the perturbation. The fastest growing wavenumber is

$$k_m = \frac{\sqrt{8\epsilon_0(1+v)}}{H_e} \quad (30)$$

and the corresponding growth rate is
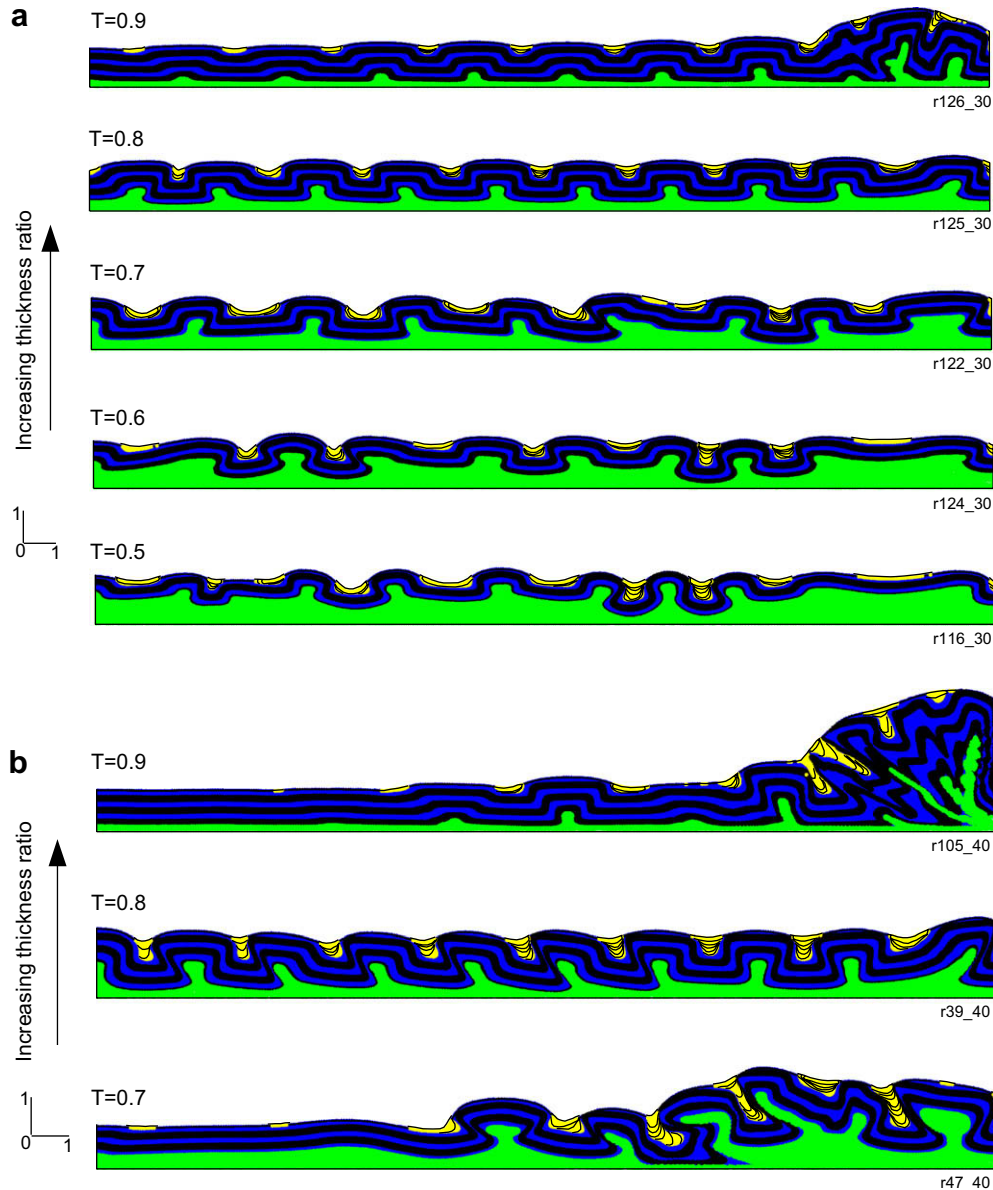
Fig. 6. Influence of the thickness of the upper competent layer relative to that of the décollement horizon (**T**) on deformation in 2 sets of experiments (parameter values are listed in Table 2). In (a) folding is favored when the décollement horizon is thick (i.e., small **T**), whereas faulting dominates when it is thin (cross-sections show deformation after 30% convergence). The simulations in (b) show deformation after 40% convergence and were carried out with a greater elastic shear resistance (**S** = 0.46) than those shown in (a) where **S** = 0.23. As the décollement horizon becomes thin (i.e., small **T**) the surface slope of the wedge increases because the viscous material has increasing difficulty in flowing to accommodate deformation of the upper competent layer.

$$\alpha_{\mathrm{m}} = \frac{16E}{9\mu(1-\nu^2)}\left(\epsilon_0(1+\nu)\frac{H_v}{H_e}\right)^3 \tag{31}$$

Equation (31) shows that the fastest growing wavelength increases as a function of the elastic resistance, the thickness ratio H_v/H_e and the initial compressive strain while it decreases as a function of the viscosity of the décollement horizon. For example, if the décollement has a low viscosity, viscous deformation can take place rapidly over considerable distances enabling perturbations in the upper competent unit to amplify. However, as the décollement becomes thin, the viscous material has increasing difficulty in flowing to accommodate deformation of the competent layer. These predictions are in qualitative agreement with, and provide an explanation for, the trends observed in numerical simulations outlined above (see Section 3.1). Although the effects of gravity have been neglected in the derivation of these results, other studies (e.g., Biot, 1961; Schmalholz et al., 2002) have shown that gravity has a stabilizing effect on folding. Once again this is consistent with the numerical simulations in that folding dominates when the total sequence thickness is small, but that as the thickness is increased, faulting dominates because fold amplification rates decrease.

How large does the fold growth rate has to be in order for folding to dominate over faulting? A preliminary analysis of this question can be addressed by comparing the time needed for rapid fold amplification with the time necessary to generate faults. The time required for a given amplification due to folding t_f is given by

$$t_{\mathrm{f}} = \frac{1}{\alpha_{\mathrm{m}}}\ln A \tag{32}$$
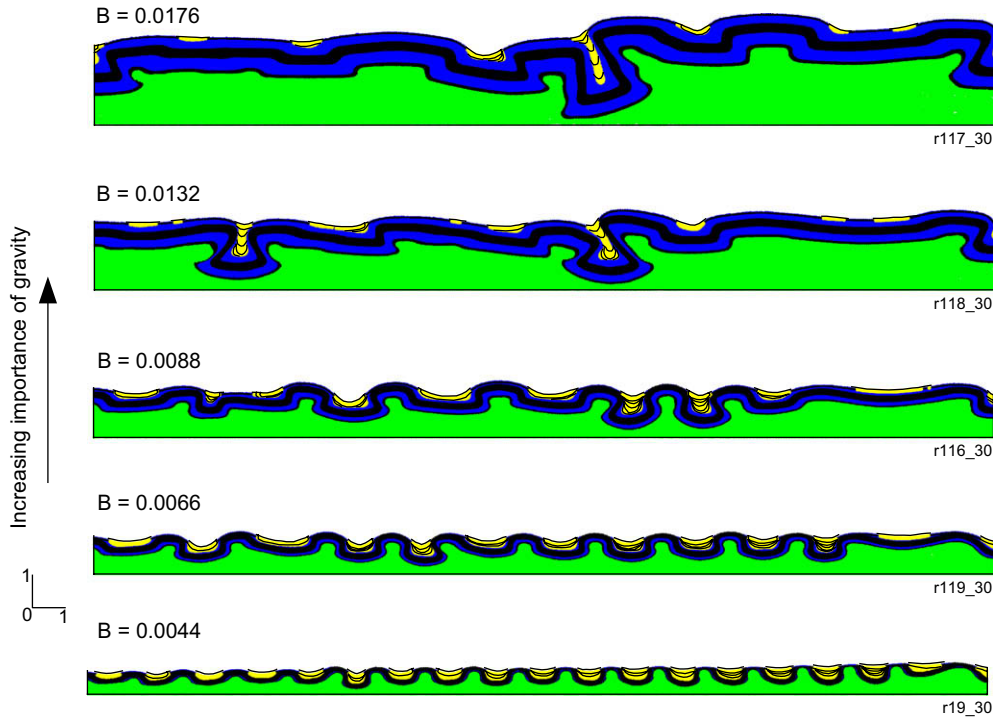
Fig. 7. Influence of the importance of gravity on deformation after 30% convergence for 5 different simulations. While folding dominates when the total thickness of the deforming section is small, faulting dominates as gravity becomes more important (i.e., at larger scales). Parameter values are listed in Table 2.

where α_m is the maximum growth rate, A is the amplification factor (i.e., the ratio of the amplitude to the initial amplitude) and ln is the natural logarithm. The amplitude factor A must be sufficiently large for folding to occur (e.g., $A = 1000$ for explosive folding, Biot, 1961). Introducing Equation (31) into (32) leads to

$$t_f = \frac{9}{16} \frac{\mu(1-\nu^2)H_e^3 \ln(A)}{E\epsilon^3(1+\nu)^3 H_v^3} \tag{33}$$

This time can be compared with the characteristic faulting time which can be estimated as the time needed for elastic stresses to build up everywhere to the Mohr–Coulomb failure envelope (from an initially unstressed state). Consider an elastic material under plane strain conditions for which the stress–strain relations are

$$\sigma_1 = \left(\frac{E\nu}{(1+\nu)(1-2\nu)} + \frac{E}{1+\nu}\right)\epsilon_1 + \frac{E\nu}{(1+\nu)(1-2\nu)}\epsilon_2 \tag{34}$$

$$\sigma_2 = \left(\frac{E\nu}{(1+\nu)(1-2\nu)} + \frac{E}{1+\nu}\right)\epsilon_2 + \frac{E\nu}{(1+\nu)(1-2\nu)}\epsilon_1 \tag{35}$$

where E is Young's modulus, ν is Poisson's ratio, ϵ are strains and σ are stresses in the 1 (horizontal) and 2 (vertical) directions. Solving Equation (35) for ϵ_2, and substituting the result into (34) gives an equation for the horizontal stress as a function of the horizontal strain and the vertical stress:

$$\sigma_1 = \left(\frac{E\nu}{(1+\nu)(1-2\nu)} + \frac{E}{1+\nu}\right)\epsilon_1$$
$$- \frac{\nu(-\sigma_2 + \sigma_2\nu + 2\sigma_2\nu^2 + E\nu\epsilon_1)}{(1+\nu)(2\nu-1)(\nu-1)} \tag{36}$$

The horizontal stresses increase as a function of compressive strain until the elastic limit is attained. The maximum horizontal stress at the Mohr–Coulomb failure surface is given by:

$$\sigma_1 = \frac{1+\sin\phi}{1-\sin\phi}\sigma_2 + \frac{2c\cos\phi}{1-\sin\phi} \tag{37}$$

where ϕ is the angle of internal friction and c is the rock cohesion. Equating Equations (36) and (37), assuming the maximum vertical stress is given by the lithostat (i.e., $\sigma_2 = \rho g(H_e + H_v)$, introducing the horizontal strain rate ($\dot\epsilon = \epsilon/t_p$) and solving for t_p yield a relation for the time for stresses at the base of the entire sequence to build up to the failure surface

$$t_p = \frac{(1+\nu)(2\nu-1-\sin\phi)\rho g(H_e + H_v)}{\dot\epsilon E(\sin\phi - 1)}$$
$$+ \frac{\cos\phi(1+\nu)(2c\nu - 2c)}{\dot\epsilon E(\sin\phi - 1)} \tag{38}$$

The plastic time t_p increases as a function of the total thickness, the cohesion and the angle of internal friction whereas it decreases as a function of Young's modulus and the strain rate. Note that a similar relation for t_p was derived by Gerbault (2000).

These results can be interpreted as follows. If $t_f < t_p$ one can expect folding to dominate over faulting due to the rapid nature of the folding instability. On the other hand, when $t_f > t_p$, the folding instability is so slow that faulting will occur before significant fold growth can occur. The boundary between faulting and folding can be found by equating Equations (33) and (38) (i.e., $t_f = t_p$). This boundary is illustrated in Fig. 12 as a function of the thickness ratio and the normalised viscosity in the ductile layer. Folding is favored when the lower ductile layer is relatively thick and has a relatively low viscosity whereas the converse is true for faulting. Though this boundary should be viewed as schematic, since it is based on a simplified model which has many parameters, it is nevertheless consistent with, and therefore helps to interpret, results of the numerical simulations.

This work is generally consistent with previous work focusing on folding versus faulting. For example, Erickson (1996) showed
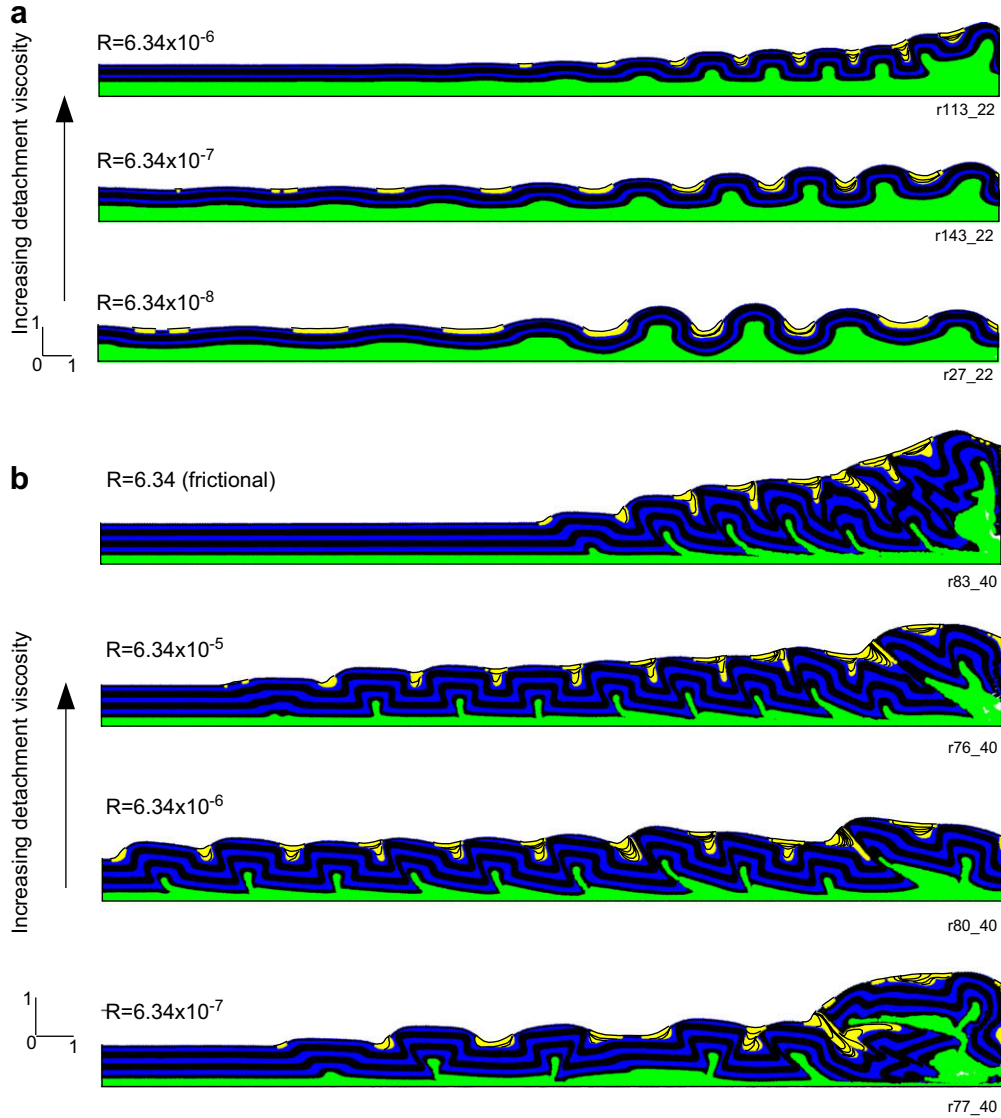
Fig. 8. Influence of the décollement viscosity **R** on deformation for two sets of simulations (parameter values are listed in Table 2). In (a) which shows deformation after 22% convergence, folding dominates when the viscosity is low, whereas the deformation is more fault-like for higher viscosities. The simulations in (b) were carried out with $\phi_b = 0$ and with a thicker cover sequence (i.e., **T** = 0.85) than in (a). In this case, deformation is always accommodated by faulting (cross-sections show deformation after 40% convergence). Low viscosities in the décollement zone favor low overall surface slopes and more symmetrical structures (including forethrusts and backthrusts) than the purely frictional (i.e., high viscosity) case.
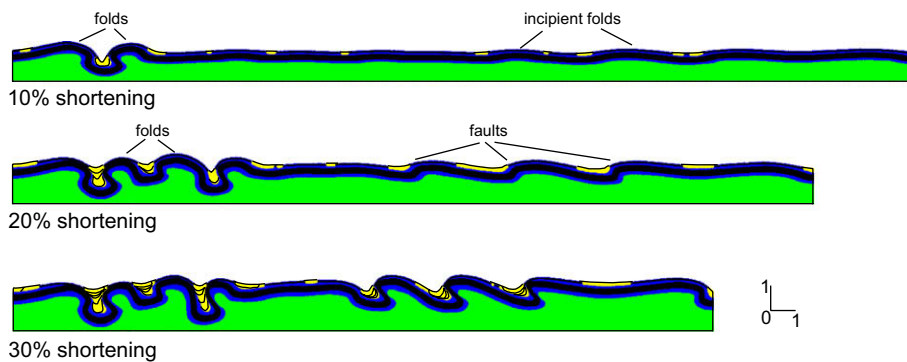
Fig. 9. Deformed cross-sections after 10, 20 and 30% of convergence (no vertical exaggeration) illustrating complex deformation consisting of both faulting and folding at different times and places. Parameter values are listed in Table 2.
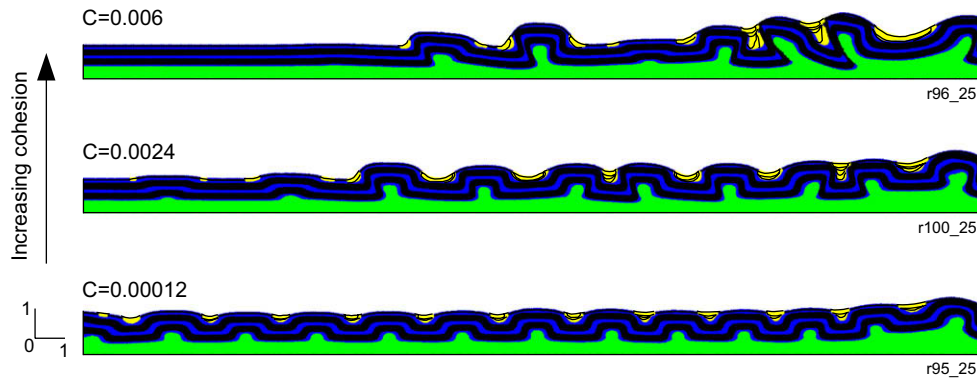
Fig. 10. Influence of varying the cohesive rock strength on the style of deformation for 3 different simulations (after 30% convergence). As the rocks become more cohesive, strain on individual structures becomes more localised (resulting in deeper basins and more elevated anticlines) and the total width of the deformation belt decreases. Parameter values are listed in Table 2.

that for elastic–plastic materials, large strength contrasts and thick, weak décollement layers favor folding due to rapid fold amplification. Similar conclusions were also reached by Johnson (1980) though he studied layers embedded within an infinite media and thus had no influence on the thickness of a lower detachment horizon. Using a somewhat different approach, Jamison (1992) postulated that the fold–thrust style which develops reflects a fundamental competition between folding and thrusting and depends on which instability surface is intersected first along any given stress path. He suggested that the buckling surface is likely to be the initial intersect of the stress path only at relatively shallow burial depths. At greater depths, the faulting instability surface is more likely to be the initial intersect. This suggestion has been confirmed within this work. In a field-based study, Pfiffner (1993) suggested that one of the most important parameters governing folding versus faulting is the thickness ratio of the mechanically weak to strong layers (see also Wissing et al., 2003). He showed that a low ratio favors imbricate thrusting and harmonic folding whereas a high value favors detachment and disharmonic folding. Once again, these results are broadly consistent with the present study.

Results are consistent with the occurrence of fold belts in areas such as the Zagros where relatively resistant carbonate rocks overlie a thick salt layer (Davis and Engelder, 1985). However, since several conditions must be satisfied in order for folding to dominate, faulting is also expected to be commonly observed in such regions, as is typically the case.

An unexpected result of this work is the importance of elasticity in governing the style of deformation. As noted above, folding requires not only a weak detachment but also that the cover rocks have a relatively high elastic shear modulus (amongst other factors). This may explain why it is typical to observe faults not folds in analogue modelling studies involving sand (which has no significant elastic behaviour) resting on a low viscosity décollement (e.g., Costa and Vendeville, 2002; Bonini, 2007).

5. Conclusions

Mechanical modelling has been used to investigate controls on folding versus faulting when layered visco-elasto-plastic sedimentary sequences are subjected to layer-parallel compression. Results indicate that folding is the dominant mode of deformation when fold amplification rates are rapid. This occurs when (1) the décollement layer is thick relative to the cover sequence (2) the décollement layer has a low viscosity (3) the cover sequence has a high elastic shear modulus and (4) the total thickness of the entire sequence is relatively small (i.e., the influence of gravity is minimal). If any of these conditions are not satisfied, fold amplification rates will be so slow that stresses will reach the failure envelope before significant fold amplification occurs. In this case, faulting is predicted to be the dominant mode of deformation.

These results indicate that the nature of deformation that develops reflects the competition between two fundamentally different instabilities: folding and faulting. Whereas faulting can be
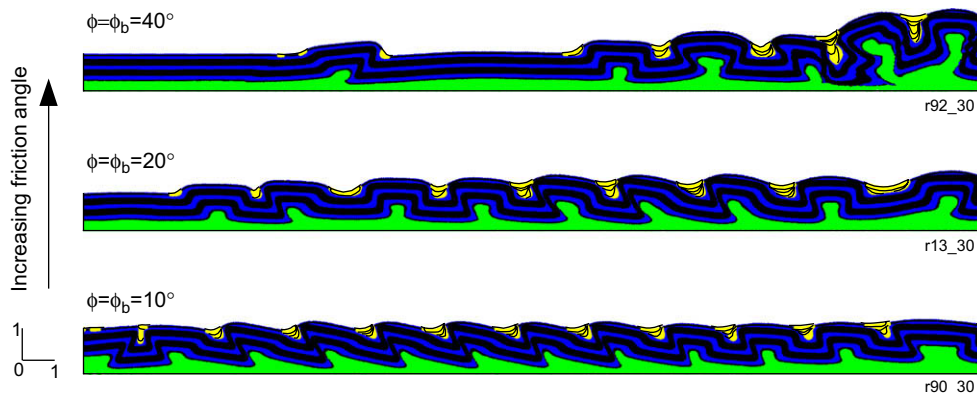
Fig. 11. Influence of the angle of internal friction (including upper competent unit and décollement) on the style of deformation after 30% convergence. Increasing the friction angle causes deformation to become more localised and for the vergence on individual structures to be more varied. Parameter values are listed in Table 2.
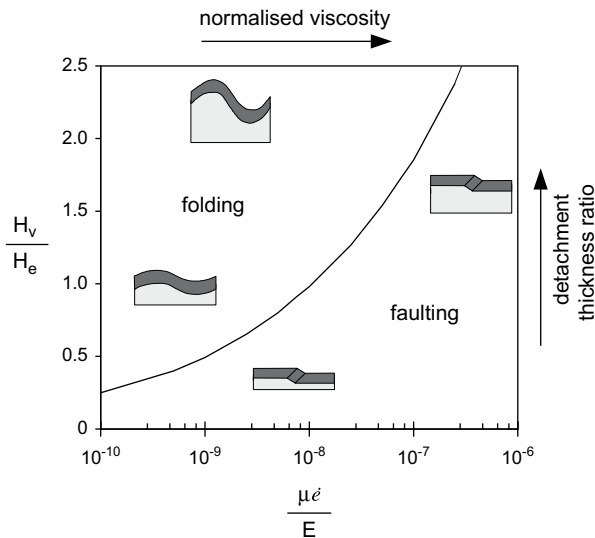
Fig. 12. Phase diagram showing the boundary between folding and faulting as a function of the thickness ratio H_v/H_e and the normalised viscosity of the décollement zone. Folding dominates when the viscous layer H_v has a low viscosity and is thick relative to the thickness overlying elastic layer H_e whereas faulting is favored by high viscosities and thin viscous décollement zones. The boundary is based on a simplified model obtained by equating relations (33) and (38) using the following parameter values: $g = 9.8$ m^2 s^{-1}, $\epsilon = 0.01$, $A = 1000$, $\dot{e} = 10^{-15}$ s^{-1}, $E = 10^{10}$ Pa, $\nu = 0.3$, $c = 0$, $\rho = 2500$ kg m^{-3}, $\phi = 30$, $H_e = 1500$ m.

viewed as the default mode, folding tends to require special conditions, such as large strength contrasts and thick, low strength décollement zones. This provides an explanation for why even when deformation occurs above a thick viscous (e.g., salt) detachment, faulting may be commonly observed.

Acknowledgments

References

Biot, M.A., 1961. Theory of folding of stratified viscoelastic media and its implications in tectonics and orogenesis. Geological Society of America Bulletin 72, 1595–1620.

Bonini, M., 2007. Deformation patterns and structural vergence in brittle–ductile wedges: an additional analogue modelling perspective. Journal of Structural Geology 29, 141–158.

Chester, J.S., 2003. Mechanical stratigraphy and fault–fold interaction, Absaroka thrust sheet, Salt River Range, Wyoming. Journal of Structural Geology 25, 1171–1192.

Chester, J.S., Chester, F.M., 1990. Fault-propagation folds above thrusts with constant dip. Journal of Structural Geology 12, 903–910.

Costa, E., Vendeville, B.C., 2002. Experimental insights on the geometry and kinematics of fold–thrust belts above weak, viscous evaporitic décollement. Journal of Structural Geology 24, 1729–1739.

Cotton, J.T., Koyi, H.A., 2000. Modeling of thrust fronts above ductile and frictional detachments: applications to structures in the Salt Range and Potwar Plateau, Pakistan. Geological Society of America Bulletin 112, 351–363.

Culling, W.E., 1964. Theory of erosion on soil covered slopes. Journal of Geology 72, 230–254.

Dahlstrom, C.D.A., 1990. Geometric constraints derived from the law of conservation of volume and applied to evolutionary models for detachment folding. Bulletin of the American Association of Petroleum Geologists 74, 336–344.

Davis, D.M., Engelder, T., 1985. The role of salt in fold-and-thrust belts. Tectonophysics 119, 67–88.

Davis, D.M., Lillie, R.J., 1993. Changing mechanical response during continental collision: active examples from the foreland thrust belts of Pakistan. Journal of Structural Geology 16, 21–34.

Dixon, J.M., Liu, S., 1992. Centrifuge modelling of the propagation of thrust faults. In: McClay, K.R. (Ed.), Thrust Tectonics. Chapman and Hall, London, p. 5369.

Erickson, S.G., 1996. Influence of mechanical stratigraphy on folding vs faulting. Journal of Structural Geology 18, 443–450.

Fakhari, M., 1994. Geological Quadrangle Map of Iran. 1:250,000 Series, No. F-12 (Khormoj Sheet). National Iranian Oil Company, Exploration Geological Division, Tehran.

Fischer, M.P., Woodward, N.B., Mitchell, M.M., 1992. The kinematics of break-thrust folds. Journal of Structural Geology 14, 451–460.

Gerbault, M., Burov, E.B., Poliakov, A.N.B., Daigni'eres, M., 1999. Do faults trigger folding in the lithosphere? Geophysical Research Letters 26, 271–274.

Gerbault, M., 2000. At what stress level is the central Indian Ocean lithosphere buckling? Earth and Planetary Science Letters 78, 165–181.

Gerya, T., Yuen, D.A., 2003. Characteristic-based marker-in-cell method with conservative finite difference schemes for modelling general flows with strongly varying transport properties. Physics of Earth and Planetary Interiors 140, 293–318.

Goff, D.F., Wiltschko, D.V., Fletcher, R.C., 1996. Décollement folding as a mechanism for thrust-ramp spacing. Journal of Geophysical Research 101, 11341–11352.

Gwinn, V., 1964. Thin-skinned tectonics in the Plateau and North western Valley and Ridge provinces of the central Appalachians. Bulletin of the Geological Society of America 75, 863–900.

Harris, L.D., Milici, R.C., 1977. Characteristics of thin-skinned style of deformation in the southern Appalachians, and potential hydrocarbon traps. U.S. Geological Survey Professional Paper, 1018.

Huang, R., Suo, Z., 2002a. Wrinkling of a compressed elastic film on a viscous layer. Journal of Applied Physics 91, 1135–1142.

Huang, R., Suo, Z., 2002b. Instability of a compressed elastic film on a viscous layer. International Journal of Solids and Structures 39, 1791–1802.

Jamison, W.R., 1987. Geometric analysis of fold development in overthrust terranes. Journal of Structural Geology 9, 207–219.

Jamison, W.R., 1992. Stress controls on fold–thrust style. In: McClay, K.R. (Ed.), Thrust Tectonics. Chapman and Hall, London, pp. 155–164.

Johnson, A.M., 1980. Folding and faulting of strain-hardening sedimentary rocks. Tectonophysics 62, 251–278.

Laubscher, H.P., 1977. Fold development in the Jura. Tectonophysics 37, 337–362.

Marques, F.O., 2008. Thrust initiation and propagation during shortening of a 2-layer model lithosphere. Journal of Structural Geology 30, 29–38.

Moresi, L., Dufour, F., Mühlhaus, H.-B., 2003. A lagrangian integration point finite element method for large deformation modelling in viscoelastic geomaterials. Journal of Computational Physics 184, 476–497.

Pfiffner, O.A., 1993. The structure of the Helvetic nappes and its relation to the mechanical stratigraphy. Journal of Structural Geology 15, 511–521.

Philippe, Y., 1994. Transfer zone in the southern Jura Thrust Belt (eastern France): geometry, development and comparison with analogue modelling experiments. In: Mascle, A. (Ed.), Hydrocarbon and Petroleum Geology of France, vol. 4. Special Publication of the European Association of Petroleum Geologists, pp. 327–346.

Schmalholz, S.M., Podladchikov, Y.Y., Burg, J.-P., 2002. Control of folding by gravity and matrix thickness: implications for large scale folding. Journal of Geophysical Research 107, doi:10.1029/2001JB000355.

Sepehr, M., Cosgrove, J., Moieni, M., 2006. The impact of cover rock rheology on the style of folding in the Zagros fold–thrust belt. Tectonophysics 427, 265–281.

Simpson, G.D.H., 2006. Modelling interactions between fold–thrust belt deformation, foreland flexure and surface mass transport. Basin Research 18, 125–143.

Smit, J.H.W., Brun, J.P., Sokoutis, D., 2003. Deformation of brittle–ductile thrust wedges in experiments and nature. Journal of Geophysical Research 108, doi:10.1029/2002JB002190.

Sulsky, D., Zhou, S.-J., Schreyer, H.L., 1995. Application of particle-in-cell method to solid mechanics. Computer Physics Communications 87, 236–252.

Suppe, J., Medwedeff, D.A., 1984. Fault-propagation folding. Geological Society of America Abstracts with Programs 16, 670.

Suppe, J., 1983. Geometry and kinematics of fault-bend folding. American Journal of Science 283, 684–721.

Wissing, S.B., Ellis, S., Pfiffner, O.A., 2003. Numerical models of Alpine-type cover nappes. Tectonophysics 367, 145–172.

Zienkiewicz, O.C., Taylor, R.L., 2000. In: The Basis. The Finite Element Method, vol. 1. Butterworth-Heinemann, Boston.